Scaling of the time-mean characteristics in the polygonal cylinder near-wake

Qing-Yang Wang[1, 2].   Sheng-Jin Xu[1*].   Lian Gan[3*].   Wei-Guo Zhang[4].   Yu Zhou[5]

Abstract

The near wake of the polygonal cylinder with the side number $N = 3 \sim \infty$ is systematically studied based on particle image velocimetry (PIV) and load-cell measurements. Each cylinder is examined for two orientations, with either one leading side or leading corner. The Reynolds number $Re = (1.0 \sim 6.0) \times 10^4$, defined by the longitudinally projected cylinder width. The dependence of the wake characteristic parameters on the cylinder orientation and N is discussed, and wake scaling analysis is conducted based on these parameters. It is found that the velocity deficit and half width of the wake scale well with the reverse flow zone length and recirculation bubble width, whilst the Strouhal number, drag and fluctuating lift coefficients scale well with the vortex formation length and wake width. The unveiled scaling relationships cast insight into the intrinsic physical connections between the aerodynamic forces and vortex formation and between the polygonal cylinder wakes of $N = 3 \sim \infty$, suggesting that the understanding of the time-mean wake behind individual polygonal cylinder can be unified to that of the circular cylinder wake.

1 Introduction

Polygonal cylinders find their applications in various engineering areas, e.g. fluid machineries, power generation systems, architecture and ocean engineering. The flow around polygonal cylinders exhibits well-known bluff-body aerodynamic features, such as laminar–turbulent transition, flow separation, vortex formation, and vortex shedding, leading to the well-known Karman vortex street under the effects of the so-called local absolute instability and global convective

✉ Sheng-Jin Xu
   xu_shengjin@tsinghua.edu.cn
✉ Lian Gan
   lian.gan@durham.ac.uk

1   AML, School of Aerospace Engineering, Tsinghua University, 100084, China
2   China Automotive Engineering Research Institute Co., Ltd., Chongqing, 401122, China
3   Department of Engineering, Durham University, DH1 3LE, UK
4   China Aerodynamics Research and Development Center, 621000, China
5   Institute for Turbulence-Noise-Vibration Interaction and Control, Harbin Institute of Technology (Shenzhen), 518050, China

instability (Tian et al. 2011; Kim et al. 2015; Huerre and Monkewitz 1990). It has been widely acknowledged that there exists a limited region of absolute instability behind the circular cylinder, where any disturbance is exponentially amplified leading to global instability in the entire wake. This region of absolute instability is responsible for the vortex formation, frequency selection, and hence the base pressure on the cylinder. The motion of the vortices in the wake is then governed by the equation of convective instability (Triantafyllou et al. 1986; Monkewitz and Nguyen 1987; Unal and Rockwell 1988). It is expected that the two types of instability play an important role in flows around polygonal cylinders because of their similar cylinder-type geometries. However, owing to the discretized side number N, the polygonal cylinders are featured with the periodically arranged flat surfaces and apexes, which strongly influence the flow separation point and separation angle, and hence the near wake as well as the extent of the absolute instability region. Eventually, the vortex shedding behaviors differ from one to another. So do the fluid forces on the cylinders and the signatures of the wakes from those of a circular cylinder. It is therefore of fundamental interest to understand how the polygonal

cylinders differ in their wake characteristics from that of the circular cylinder and how they depend on N. For instance, the polygonal cylinder with $N \leq 8$ is generally characterized by the flow separation points fixed at their corners, which are insensitive to the Reynolds number (Re), and the laminar–turbulent transition does not occur over a wide Re range, e.g. $(1.0 \sim 6.0) \times 10^4$. The drag on a polygonal cylinder of finite N is in general larger than that on a circular cylinder ($N = \infty$) in the subcritical flow regime. Given $N \geq 12$, the critical Reynolds number Re_c where the transition to turbulence starts to occur in the boundary layer is smaller than, though approaching with increasing N, that of the circular cylinder (Xu et al. 2017).

The near wake of cylinders, be square or circular cross-section, be single or two, is often characterized by the vortex formation length L_f^* and the wake width D_w^*, where asterisk denotes normalizations by cylinder characteristic width D (e.g. Bloor 1964; Gerrard 1966; Griffin 1995; Alam et al. 2011; Wang et al. 2018). It has been established that the two characteristic length scales, St and the fluid forces on the cylinder are correlated (Cetiner and Rockwell 2001; Carberry et al. 2001). Hu et al. (2006) investigated the effect of the corner radius of a square cylinder on the wake. They found that L_f^* was gradually prolonged with increasing corner radius, whereas the wake half width $\delta_{1/2}$ shrank. They concluded that the variation of L_f^* and $\delta_{1/2}$ depended on the flow separation angle which was determined by the curvature of the corner. It seems plausible that there exists interrelationship between the fluid forces, St, L_f^*, $\delta_{1/2}$ and flow separation angle.

However, this interrelationship between fluid forces and wake structures and its dependence on N have not been systematically studied and have yet to be unveiled for the polygonal cylinder wake. Other issues such as the general characteristics of the mean velocity and Reynolds stresses in the near field, their downstream evolution and correlations with the fluid forces, especially their dependence on N, are also of fundamental and practical importance. A thorough understanding of these issues may provide an important reference to wake instability studies. In this work, we aim to address the above issues based on extensive particle image velocimetry (PIV) and fluid forces measurements. Experimental details are given in Section 2. Statistical quantities and scaling analysis of the polygonal cylinder wake are presented in Section 3. Finally, the main conclusions are summarized in Section 4

2 Experimental Details

Experiments were conducted in an open-circuit low-speed wind tunnel with a square working section of 0.5m×0.5m×2.0m. The flow speed U_∞ within the test section ranges from 2m/s to 40m/s and the streamwise turbulence intensity is less than 0.5% for the velocity range of the present concern. The polygonal cylinder was mounted horizontally in the symmetry plane of the working section, as shown in Fig. 1 where a hexagonal cylinder was installed. Two large thin plates were attached at the ends of the cylinder in order to suppress the end effect. The test models included the polygonal cylinders of side number $N = 3 \sim 8$, 12, 16 and a circular cylinder ($N = \infty$). Measurements were conducted for two orientations of each polygonal cylinder, with either a leading corner or a leading side (see Fig. 1 for notations and abbreviations). In order to obtain the same Re at the same U_∞ and the same blockage ratio for all cylinders, two sets of cylinder models were designed for the polygons of even N to ensure $D = 25$mm for both corner and face orientations (Fig. 1). For odd N, one set of model is adequate as its two orientations are associated with the same D. The blockage of all polygonal cylinders is 5%. The cylinder length L between the two end plates was 420mm, giving an aspect ratio $L/D = 16.8$, at which the blockage as well as the three-dimensional end effect is negligible. The Reynolds number, $Re = U_\infty D/v$, is $(1.0 \sim 6.0) \times 10^4$, where v is the kinematic viscosity of air.

The flow field behind the cylinder was measured using a standard LaVision planar PIV system. Flow illumination was provided using a double-pulsed Nd-YAG Laser source with a wavelength of 532nm and a maximum energy output of 120mJ per pulse. A high sensitivity Imager Pro X CCD camera with a resolution of 2048 pixels × 2048 pixels was deployed together with a Nikon 50mm (f: 1.8) objective lens. Flow was seeded with smoke particles of about 1 μm in diameter,

generated from paraffin oil via Laskin nozzles.

The origin of the coordinate system is at the center of the polygonal cylinder (Fig. 1). The field of view (FOV) was fixed at $-0.8 \lesssim x/D \lesssim 8.0$ and $-2.0 \lesssim y/D \lesssim 2.0$. The sampling rate of PIV was 4 Hz, more than 1000 pairs of double-framed images for each case were taken to ensure a good convergence for all concerned statistical quantities. A careful assessment of the St values reported previously in Xu et al. (2017), measured at the same Re, indicates that the present sampling rate has no phase-locking issues for all the testing cases. That is, a random sampling was achieved at all phases of the shedding cycle. The raw PIV images were processed using DaVis 7.2, with a final interrogation window (IW) size of 32×32 pixels and 50% overlap, resulting in a spatial resolution of 1.85 mm based on the IW size.
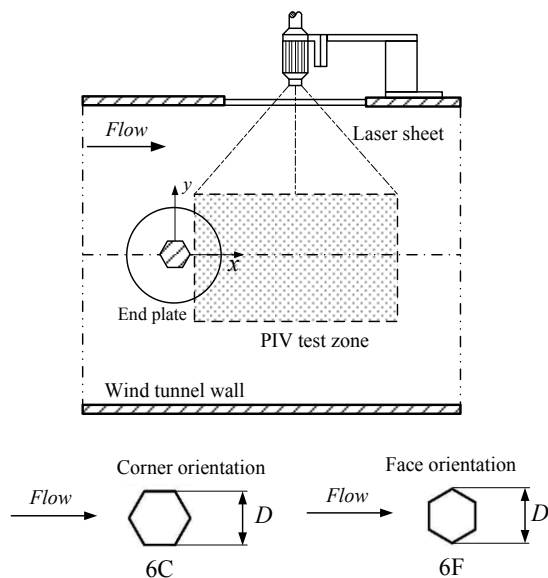

Fig. 1 Schematic of the experimental setup (not to scale), including one example of the test model and its two orientations. In the notation of NF or NC, N denotes the polygon side number and F and C stand for the face and corner orientations, respectively.

The drag and lift forces on the cylinder were measured using a load-cell (Kistler 9317B). The cylinder was fixed vertically in the wind tunnel. The cylinder was connected to the load-cell at the bottom and was supported at its upper end by a preload bolt to minimize structural vibration (Fig. 2). The force signals were amplified by a charge amplifier (Kistler 5073A) and then sampled at 5 kHz by an NI A/D (analog/digital) board (PCI - 6221) for a sampling duration of 5s. The Strouhal number is defined as $St = f_s D/U_\infty$, where f_s was the predominant vortex shedding frequency, extracted from the spectrum of the load cell signal. More information about measurement methods on aerodynamic forces and St can be found in Xu et al. (2017).
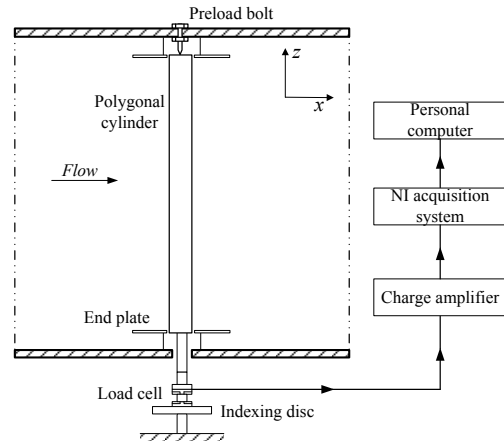

Fig. 2 Schematic of the force measurement set-up.

3 Results and discussion

3.1 Instantaneous wake structure

Fig. 3 presents the instantaneous vorticity fields $\omega_z D/U_\infty$ of representative polygonal cylinders, where $\omega_z = \partial v / \partial x - \partial u / \partial y$, and u, v are the instantaneous velocities in the x and y direction, respectively. The cylinder upper surface flow separation points are also marked on the surface of the cylinder. According to Xu et al. (2017), at this Re, the separation point on the polygonal cylinders are fixed at a corner. The separated shear layer can be seen by the large magnitude (negative) vorticity regions detached from cylinder surface after flow separation point. This separated shear layer is then rolled up from the upper and lower surfaces in an alternative manner to form the classical Karman vortex street.

The samples displayed in Fig. 3 are chosen at a similar vortex shedding phase, from which it is possible to reflect the vortex formation distance and the wake width behind the cylinder. Comparing with the circular cylinder, in NC cylinders, 4C has a large formation distance and 8C has a small one. These are in fact the largest and the smallest case, which will be discussed in details in section 3.3. In NF cases, 3F and 5F are the largest and smallest. In terms of wake width, it can be

inferred that 8C and 5F have a small wake width while 6C and 4F ($\approx$ 3F) have the largest. It is also possible to speculate the vortex strength (circulation) from these instantaneous flow fields. That is, a larger wake width could indicate stronger vortex strength.

In this study, we will focus on the vortex formation distance and wake width. Investigation of the strength of the coherent vortices is left to a future work.
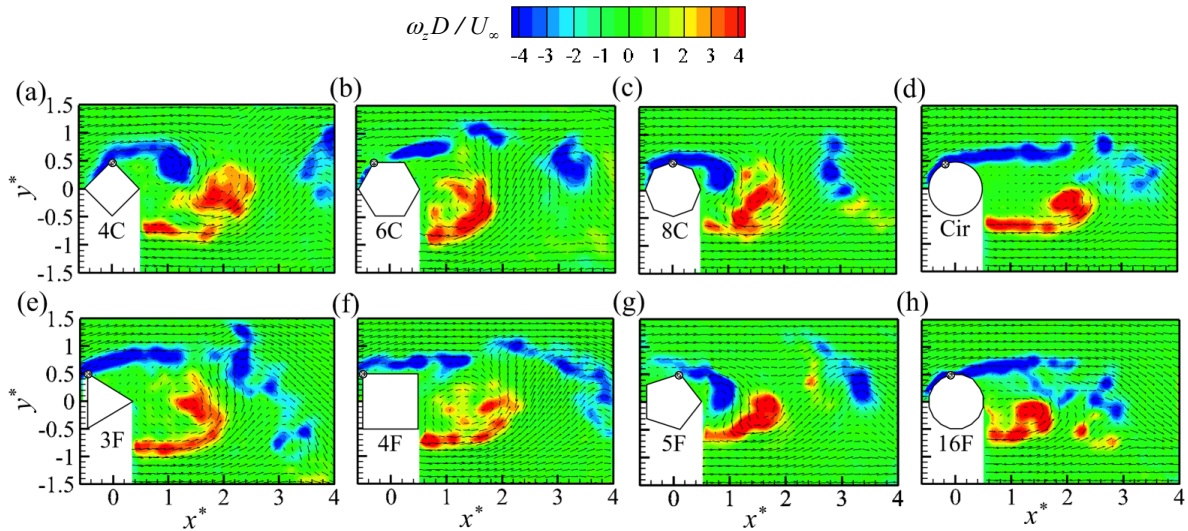

Fig. 3 Contours of the instantaneous vorticity fields overlaid with velocity vectors for representative polygonal cylinders at $Re = 1.6 \times 10^4$. The upper surface flow separation points are marked by the dots. (a) ~ (c) corner orientation; (e) ~ (h) face orientation.

3.2 Statistical characteristics of near-wake

It has been documented in Xu et al. (2017) that the transition from laminar to turbulence occurs in the boundary layer around the cylinders of $N = 12$ and 16 given $Re \geq 3 \times 10^4$. Fig. 4 presents the iso-contours of $\overline{U}$ for a few representative cylinders at subcritical Re and supercritical Re for $N = 12$ and 16. In this paper, the overbar and the prime represent the time-averaged and the fluctuating components, respectively, that is, the instantaneous flow velocities $\{u, v\} = \{\overline{U} + u', \overline{V} + v'\}$. The reverse flow zone boundary is demarcated by the contour level $\overline{U} = 0$, whose longitudinal extent is correlated with the drag on the cylinder (He et al. 2014). The configurations of 8C and 5F are characterized by a much smaller reverse flow zone than those of the circular and square cylinders at $Re = 1.6 \times 10^4$, implying smaller C_D.

The reverse flow zone contracts by typically 75% from the subcritical (Fig. 4a3, 4a6) to supercritical (Fig. 4b) cylinders due to the occurrence of the transition in the boundary layer.

The iso-contours of the streamwise Reynolds normal stress $\overline{u'u'}$ are shown in Fig. 5. The 4F case is characterized by the highest $\overline{u'u'}$ peak value of 0.18 U_∞^2 at $x^* \approx 1.5$, where the narrowest distance between the two peaks occurs. On the other hand, the cases of 8C and 5F are associated with the lowest peak value (0.12 U_∞^2) that occurs at $x^* \approx 1.2$. In the supercritical regime (12C and 16F, $Re = 5.1 \times 10^4$), the region of large $\overline{u'u'}$ contracts significantly, in line with the variation of the reverse flow zone, the peak being closest to the cylinder.
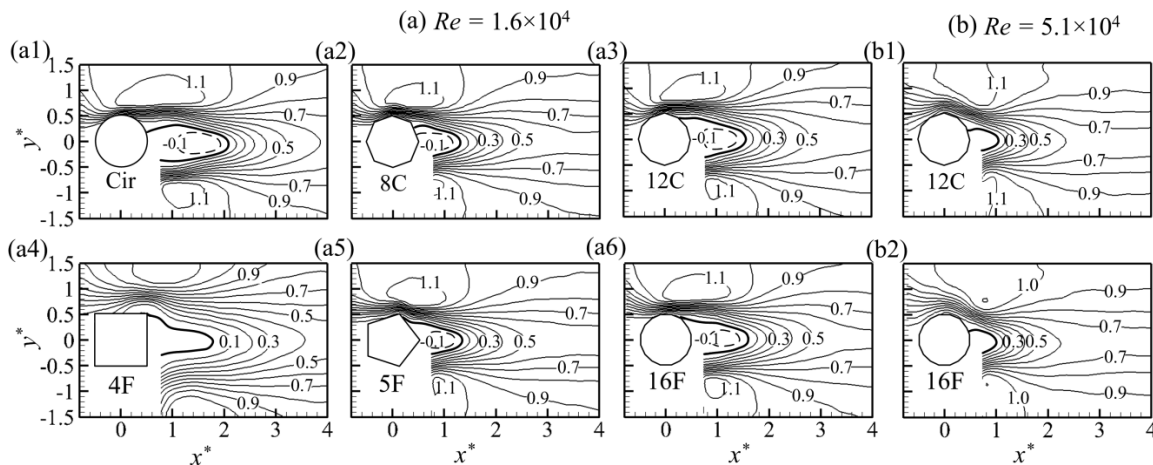
Fig. 4 Iso-contours of time-averaged streamwise velocity $\bar{U}/U_\infty$ for representative polygonal cylinders. Dashed lines denote negative level. The boundaries of the reverse flow zones, along which $\bar{U} = 0$, are highlighted by thick solid lines. The contour increment is 0.1.
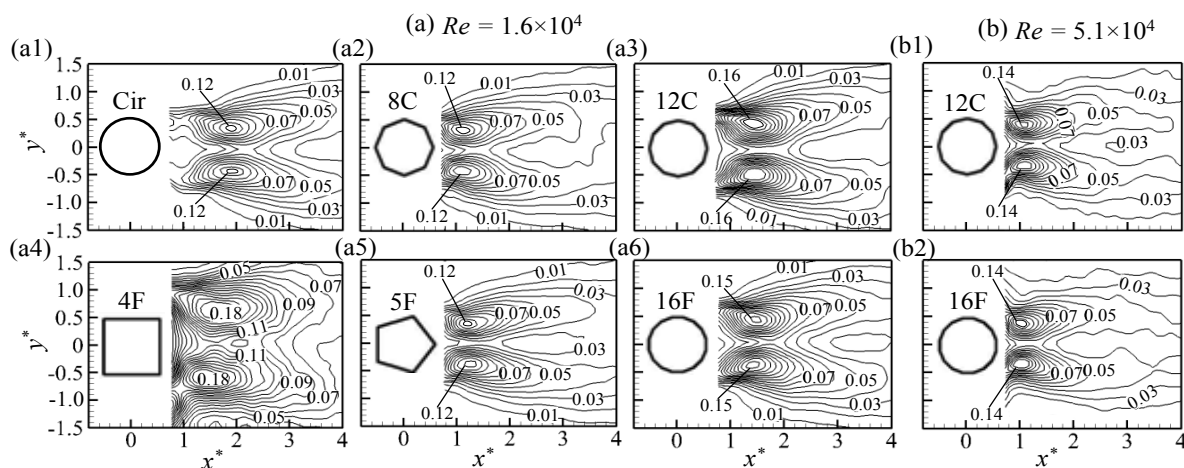

Fig. 5 Iso-contours of streamwise Reynolds normal stress $\overline{u'u'}/U_\infty^2$. The contour increment is 0.01.

The single peak on the centerline can be seen clearly in the iso-contours of $\overline{v'v'}$ (Fig. 6). It can be deduced that the oppositely signed vortices are initially convected towards the centerline before moving apart laterally, when the lateral separation between their vortex trajectories is smallest, the maximum centerline $\overline{v'v'}$ occurs. The 4F case is associated with the highest $\overline{v'v'}$ of $0.36\,U_\infty^2$ at $x^* = 2.4$. On the other hand, the peak of $\overline{v'v'}$ is smallest for the circular cylinder compared with all the other cases in the subcritical regime. As in the case of $\overline{u'u'}$, the maximum $\overline{v'v'}$ is appreciably lower and also occurs more closely to the cylinder for 12C and 16F in the supercritical regime than those in the

subcritical regime.

It will be shown that cases 4C and 3F are characterized by the largest velocity deficit or reverse flow zone length next, and 4F have the strongest streamwise and lateral velocity fluctuations (Fig. 5 and Fig. 6). On the other hand, cases 8C and 5F show the smallest velocity deficit (or reverse flow zone) and velocity fluctuations. Then, we will examine the Reynolds shear stress $\overline{u'v'}$, recirculation bubbles and mean vorticity fields focusing on these special cases at $Re = 1.6 \times 10^4$.
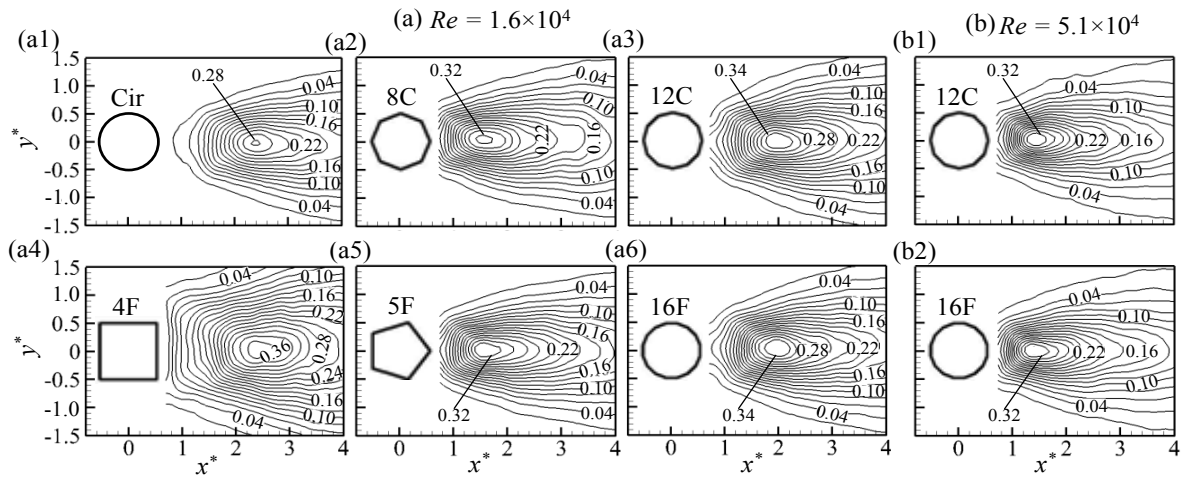
Fig. 6 Iso-contours of lateral Reynolds normal stress $\overline{v'v'}/U_\infty^2$. The contour increment is 0.02.

The $\overline{u'v'}$ contours (Fig. 7) display an anti-symmetric pattern about the centerline. The $\overline{u'v'}$ is positive above the centerline and negative below inside the reverse flow region; the signs are swapped outside. Such a four-quadrant-type pattern, originated from the generation of vortices, is the same as behind a circular cylinder (Kim et al. 2006) and a square cylinder (Qu et al. 2017). Apparently, this pattern is insensitive to the bluff body shape. The region of large $\overline{u'v'}$ outside the reverse flow region is associated with strong velocity fluctuation. The $\left|\overline{u'v'}\right|$ magnitude is largest at $x^* \approx 2$ for 6C and 4F, about $0.09\,U_\infty^2$. The maximum magnitude in $\left|\overline{u'v'}\right|$ is about $0.07\,U_\infty^2 \sim 0.08\,U_\infty^2$ for the other cases, including the circular cylinder. Note that 4C and 3F have the largest reverse flow zones for the two orientations, respectively, while 8C and 5F have the smallest. The size of the reverse flow zone of the circular cylinder and 16F falls between.
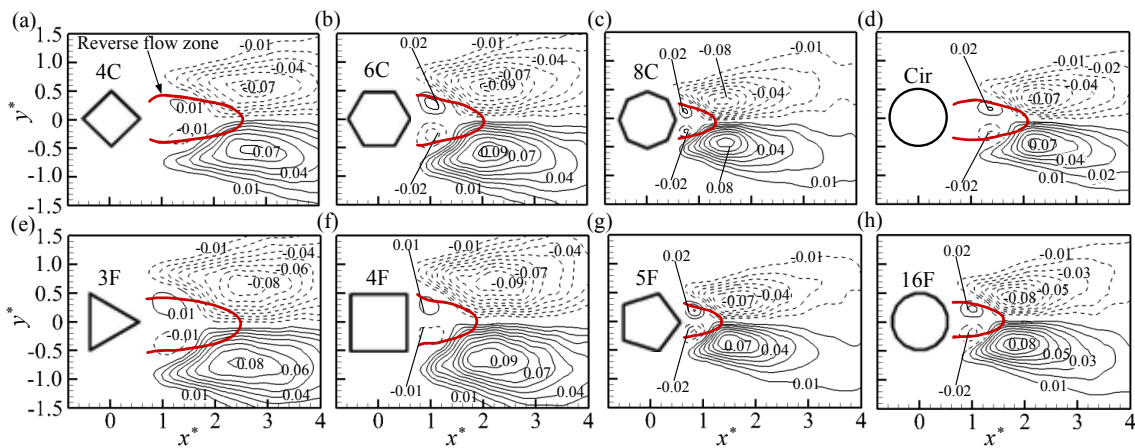

Fig. 7 Iso-contours of Reynolds shear stress $\overline{u'v'}/U_\infty^2$ and its relation to the reverse flow zone, as highlighted by a red-colored curve ($Re = 1.6\times10^4$). The contour increment is 0.01.

Fig. 8 presents the recirculation bubble defined by the separation streamline that starts at the separation point (see Fig. 3), encloses the pair of symmetrical mean recirculation zone and the mean shear layers indicated by the mean vorticity $\overline{\omega}_z D/U_\infty$, where $\overline{\omega}_z = \partial\overline{V}/\partial x - \partial\overline{U}/\partial y$. The recirculation bubbles behind 8C and 5F cylinders are markedly smaller than those behind 4C, 3F, 16F and the circular cylinder. The reverse flow zone (Fig. 7) and the recirculation bubble (Fig. 8) are different in geometry, the former passing through the center of the recirculation bubble (one on each side of the centerline), where the local velocity is zero, and the

latter tracing back to the separation points (Kim et al. 2006; Shi and Feng 2015). The mean shear layer essentially follows the recirculation bubble boundary, with the decreasing $|\bar{\omega}_z|$ downstream. Clearly, cases 8C and 5F are associated with the smallest recirculation bubble sizes and hence the smallest regions of high shear (high $|\bar{\omega}_z|$), while 4C and 3F are the opposite, showing the largest recirculation bubble and high-shear region, exceeding their counterparts of 16F and the circular

cylinder. It is interesting to find from a comparison between cases 4C and 4F that, although 4C has more streamlined windward surface and aft-body, its reverse flow zone and the recirculation bubble are both larger. Finally, it is worth pointing out that a large reverse flow zone or recirculation bubble does not necessarily mean a big region of large magnitude in $\overline{u'v'}$; this is evident if we compare the cases of 4C and 3F with 6C and 4F in Fig. 7 and Fig. 8.
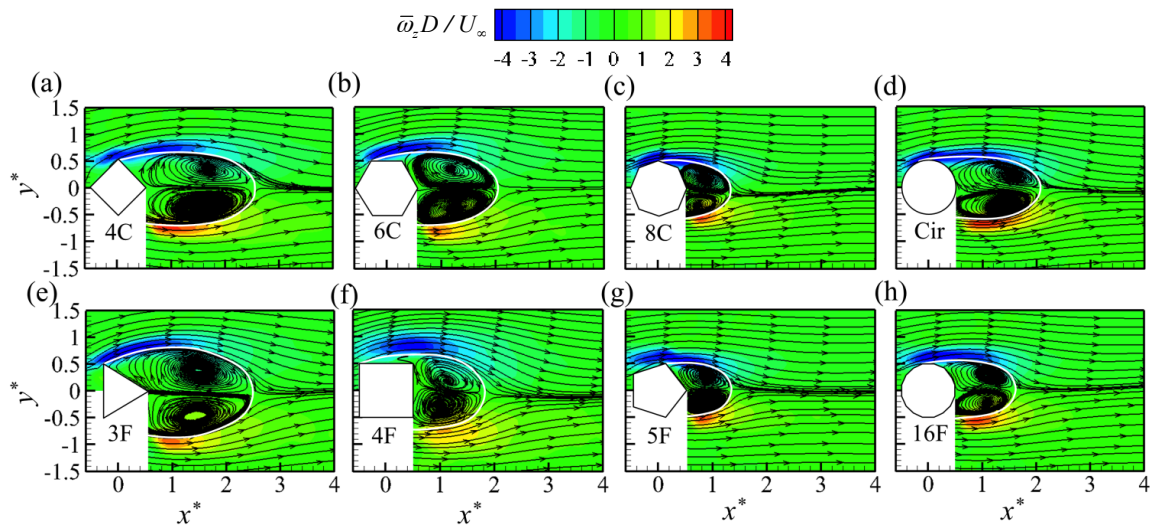

Fig. 8 Contours of the mean vorticity fields overlaid with streamlines, the white solid line encloses the recirculation bubble. Note that the asymmetry of the $\bar{\omega}_z$ contours is attributed to the laser shadow effect. ($Re = 1.6 \times 10^4$).

3.3 Wake characteristic parameters

The several wake characteristic parameters to be investigated are defined in Fig. 9 based on the statistical quantities in the wake, where the cylinder configuration 6C is shown for illustration. Following the conventions, the vortex formation length L_f is defined as the streamwise position where the root mean square (RMS) value u'_{rms} of the fluctuating streamwise velocity u' on the centerline reaches the maxima (Bloor 1964; Alam, Zhou & Wang 2011). The characteristic wake width D_w is defined to be the lateral separation between the two maxima in u'_{rms} at the position $x^* = L_f^*$ (Griffin 1995). The streamwise length L_r of the reverse flow zone is the distance from the cylinder center to the position where $\overline{U}/U_\infty = 0$ on the centerline. The recirculation bubble width D_b is defined to be the maximum distance between the two separation streamlines.
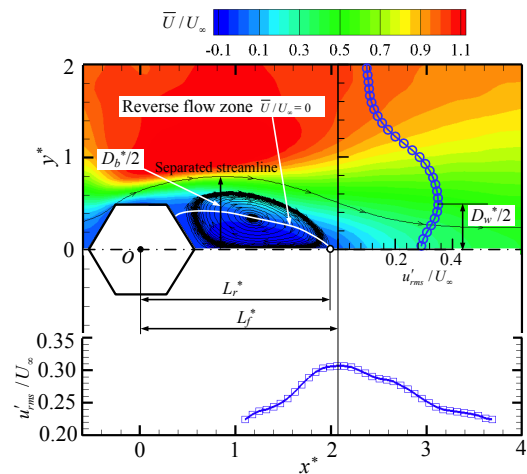

Fig. 9 Definitions of the wake characteristic parameters. The $\overline{U}$ contours, $\{\overline{U}, \overline{V}\}$ streamlines and u'_{rms} are extracted from the case 6C at $Re = 1.6 \times 10^4$.

The dependence of L_f^*, L_r^*, D_w^* and D_b^* on N and orientation is presented in Fig. 10 and Fig. 11 at different Re. It can be found that these parameters do not depend

strongly on Re. The NC and NF orientations exhibit different behaviors for $N \leq 8$. For example, for the NC case at $Re = 1.6 \times 10^4$, L_f^* shows a marginal rise and then a significant monotonic drop for $N \leq 8$. For $N > 8$, L_f^* approaches a constant of about 1.5. However, for the NF case, L_f^* drops initially until $N = 5$ and then rises above the NC cases, reaching its peak at $N = 8$. For $N \geq 12$, Re plays an important role due to the boundary layer transition. At $Re > 3 \times 10^4$, the boundary layer transition postpones the flow separation, resulting in a further decline in both L_f^* and L_r^* for $N = 12$ and 16 (the critical Reynolds numbers Re_{cr} are about 3×10^4 and 4×10^4 for

12C and 16C, respectively, according to the research of Xu et al. 2017).

Apparently, the variation of L_r^* follows closely that of L_f^*, though the former is smaller. Moreover, given for the NF orientation, L_r^* is approximately equal to L_f^* for all N, regardless of the occurrence of the transition. In contrast, for the NC orientation L_r^* appears more sensitive to the transition, which is in line with the variation of C_D and St reported in Xu et al. (2017); the difference between L_f^* and L_r^* is more pronounced as Re increases as the transition influences L_r^* more than L_f^*. This may be confirmed from Fig. 10.
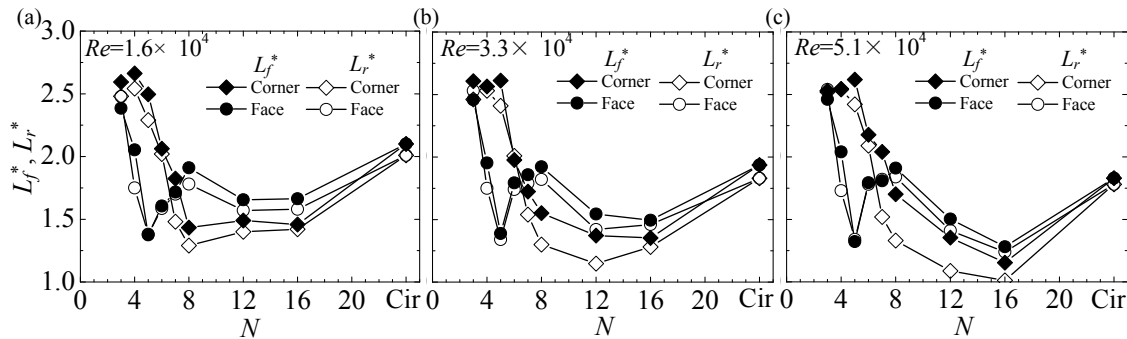

Fig. 10 Dependence on N of the vortex formation length L_f^* and the streamwise length L_r^* of the reverse flow zone for different Re.
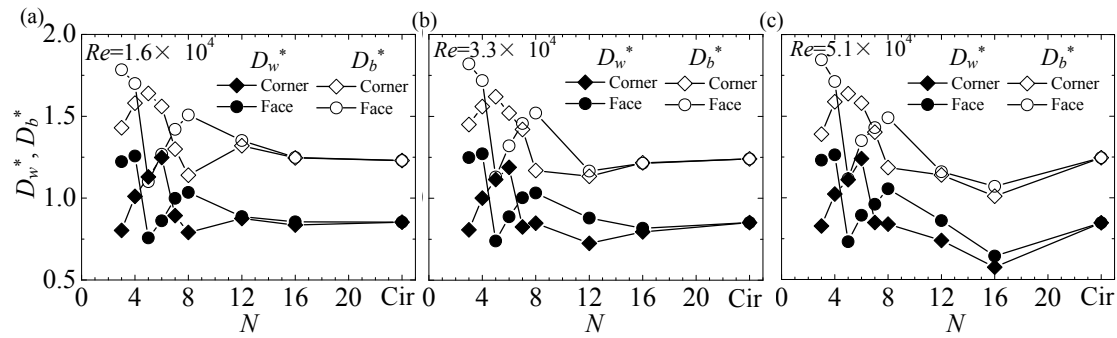

Fig. 11 Dependence on N of the wake width D_w^* and the bubble width D_b^* for different Re.

The variations in D_w^* and D_b^* with N (Fig. 11) appear similar, but the difference between D_w^* and D_b^* is larger than that between L_f^* and L_r^*, i.e., $(D_b^* - D_w^*) > (L_f^* - L_r^*)$. Again, given $N \leq 8$, the NC orientation behaves differently from the NF orientation for all Re. At $Re = 1.6 \times 10^4$, D_w^* is a strong increasing function of N for $3 \leq N \leq 6$ of the NC orientation but, after reaching the peak at $N = 6$, declines to the minimum value at $N = 8$. For the NF orientation, D_w^* reaches the minimum at $N = 5$ and then rises till $N = 8$. At larger Re, the D_w^* and D_b^* for $N = 12$ and 16 decrease further because of

the transition occurring.

3.4 Scaling analysis

Next, the scaling analysis of wake characteristics physical quantities and force coefficients is carried out according to the wake parameters discussed above.

3.4.1 Scaling of the wake characteristics

Fig. 12(a, b) compares the variation in the centerline velocity deficit $U_1(x) = U_\infty - \bar{U}_{min}(x)$ for all cylinders, where $\bar{U}_{min}(x)$ is the centreline velocity for a fixed x.

The reverse flow zone length L_r^* is the distance from the cylinder center to the second intersection point (the first being the rear stagnation point on the cylinder) between $U_1(x)/U_\infty$ and $U_1/U_\infty = 1$ where $\overline{U}_{min} = 0$, indicated by the dashed line in Fig. 12 (a, b).
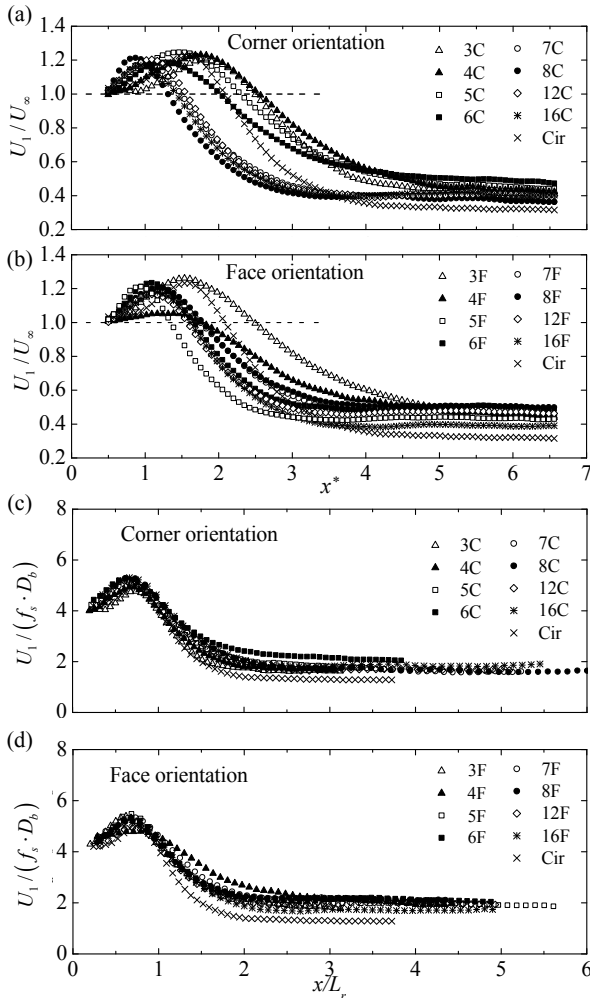

Fig. 12 (a), (b) The centerline streamwise velocity deficit U_1 in the wakes at $Re = 1.6 \times 10^4$. (c), (d) Dependence of the scaled velocity deficit $U_1/(f_s D_b)$ on x/L_r.

It can be found that the maximum $U_1 (x)$ is approximately $1.2U_\infty$ for all cylinders, irrespective of the cylinder orientation. The exception is 4F case, whose value is about $1.05U_\infty$. The 4F case is characterized by a flat surface facing normally to incoming flow and meanwhile a lack of aft-body, different from other cylinders. The velocity recovery rate is determined by $|\partial U_1 / \partial x|$ after the occurrence of the maximum U_1 ($U_{1,max}$), not necessarily proportional to L_r. In this paper, subscript max denotes the maximum value. Among the

corner orientations, case 8C has the highest recovery rate and 6C has the slowest, albeit with an intermediate L_r (Fig. 12a). On the other hand, among the face orientations, case 5F has the highest recovery rate, and 4F the slowest, although associated with a very small $U_{1,max}$ and an intermediate L_r (Fig. 12b). It can be inferred that the cases of 6C and 4F are characterized by vortices of higher strength or circulation than the others in the near wake, resulting in the lowest base pressure and velocity recovery, and 8C and 5F cases are opposite.

Monkewitz and Nguyen (1987) and Huerre and Monkewitz (1990), among others, demonstrated that the reverse flow and the velocity deficit recovery rate are closely related to the local absolute instability in the near wake, i.e. the size of this instability region is marginally larger than that of the reverse flow zone. It is therefore inferred that the cases of 8C and 5F have a smaller absolute instability region, and any source of instability originated from the boundary layer around the cylinder will have a smaller influential area to get amplified. As a result, the 8C and 5F cases are associated with a weaker instability region and hence smaller and weaker vortices. On the other hand, the cases of 6C and 4F are opposite. This is fully consistent with the discussion above.

Apparently, U_1 at a given x is very different from one cylinder to another. However, the rescaled velocity deficit $U_1/(f_s D_b)$, where D_b is recirculation bubble width, collapses reasonably well for most of the cylinders if the abscissa is scaled as x/L_r (Fig. 12c, d). As suggested by Huerre and Monkewitz (1990), U_1, L_r, D_b and f_s are the controlling parameters for the local absolute instability and the vortex shedding process of the circular cylinder, and in turn scale with the near-wake velocity deficit. Evidently, the argument is also valid for the polygonal cylinder wakes. For the same reason, L_r and D_b are used as the characteristic length scale when the wake half width $\delta_{1/2}$ is examined.

It can be found that the maximum $U_1/(f_s D_b)$ occurs at $x/L_r \approx 0.75$ in Fig. 12(c, d). Close to the cylinder ($0.75 \leq x/L_r \leq 1.5$), at the present Re range, the viscous dissipation effect should be negligibly small, the scaled

velocity deficit $U_1/(f_s D_b)$ is characterized by the same recovery rate, which suggests a similar (relative) pressure gradient and vortex shedding characteristics among all cases. In the range $1.5 < x/L_r \le 2.5$, the recovery rate of $U_1/(f_s D_b)$ shows some differences, probably due to different extent of vortex interactions there. Further downstream, for $x/L_r > 2.5$, $U_1/(f_s D_b)$ decays fairly slowly and remains in the range of $U_1/(f_s D_b)$ = 1.8 ~ 2.0 for different wakes, indicating that pressure gradient may have become negligibly small. However, the cases of 4F (square cylinder) and $N = \infty$ (circular cylinder) are exceptional. The base pressure coefficient is C_{pb} = -1.7 for 4F but only C_{pb} = -1.2 for $N = \infty$, as reported by Bearman and Obasaju (1982) and Nishimura and Taniike (2001), respectively, which represent perhaps two extreme cases. It may be inferred that the base pressure values of the polygonal cylinders are probably between that of 4F and $N = \infty$. A lower base pressure should produce a large adverse pressure gradient, hence corresponds to a slow velocity recovery rate.

Define the wake half width $\delta_{1/2}$ by the lateral distance between the two points where $U_\infty - \bar{U} = 0.5 U_1$. The $\delta_{1/2}$ decreases first to its minimum $\delta_{1/2,min}$ at $x = L_r$ (Fig. 13a, b), in line with the recirculation bubble shape behind the cylinder (Fig. 8), and then increases gradually. The $\delta_{1/2,min}$ of 4C is the largest among the corner orientations and that of 3F among the face orientations. On the other hand, 8C and 5F are characterized by the smallest $\delta_{1/2,min}$ for the corner and face orientations, respectively. Beyond $x^* = 4$, the largest $\delta_{1/2}$ occurs with 6C and 4F, and the smallest $\delta_{1/2}$ with 3C and 5F. The $\delta_{1/2}$ is also quite small for the circular cylinder.

The fact that $\delta_{1/2}$ decreases to its minimum at $x = L_r$ suggests that individual vortices behind the cylinders are convected initially inwards to the centerline until $x = L_r$ before moving outwards, although the vortices are still in the formation process in this stage, that is, they have not yet detached from the shear layer (Fig. 13a, b). This casts some light upon the fact that L_r is a streamwise scaling factor for $\delta_{1/2}$. It is found that $\delta_{1/2}$ is laterally proportional

approximately to D_b. Using the two scaling factors to scale the abscissa and ordinate, respectively, in Fig. 13(a, b), and then $\delta_{1/2}/D_b$ collapses fairly well for $x/L_r \le 2$ (Fig. 13c, d). For the range of $1 \le x/L_r \le 2$, the growth rate of $\delta_{1/2}/D_b$ is almost linear and identical for different cylinders (except the circular cylinder), apparently resulting from the same velocity recovery rate for these polygonal cylinders over this streamwise range (Fig. 13c, d). For $x/L_r > 2$, the variation rate becomes much smaller, exhibiting an obvious dependence on N and the cylinder orientation, due to the viscous dissipation and the vortex interactions downstream.
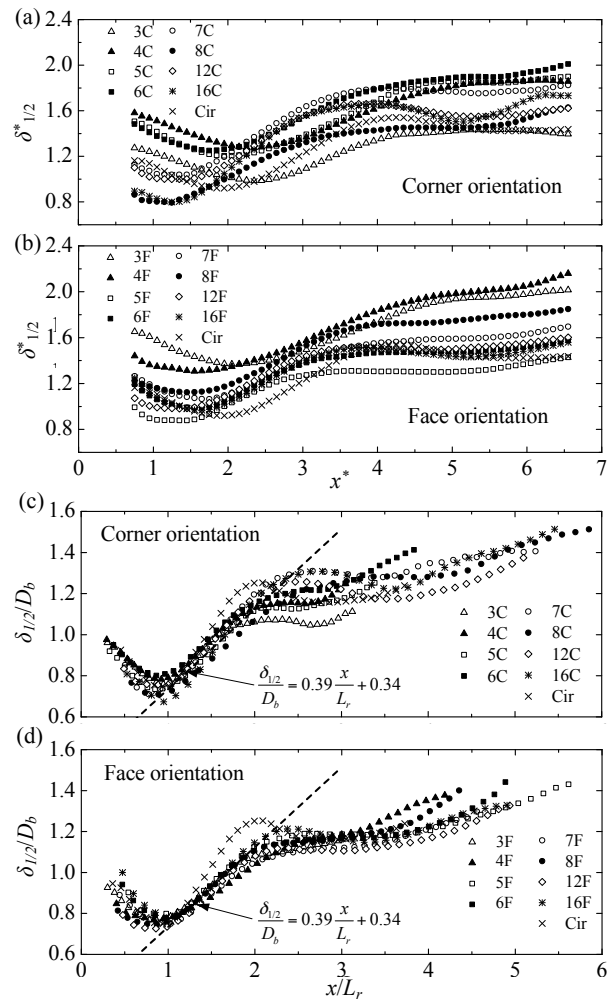

Fig. 13 (a), (b) The wake half width $\delta_{1/2}^*$ for all cylinders at $Re = 1.6 \times 10^4$. (c), (d) Dependence of D_b scaled $\delta_{1/2}$ on x/L_r. The dashed line is the straight line least-square-fitted to the data of all polygonal cylinders, excluding the circular cylinder, over $1 \le x/L_r \le 2$.

A comparison between Fig. 12(c, d) and Fig. 13(c, d)

indicates that the recirculation bubbles resemble each other if scaled with L_r and D_*, irrespective of the corner or face orientation, at least for the Re range examined. The result suggests that 8C and 5F are associated with the smallest size of the recirculation bubble and of absolute instability region, which directly account for the weakest strength of the vortices in the near wake.
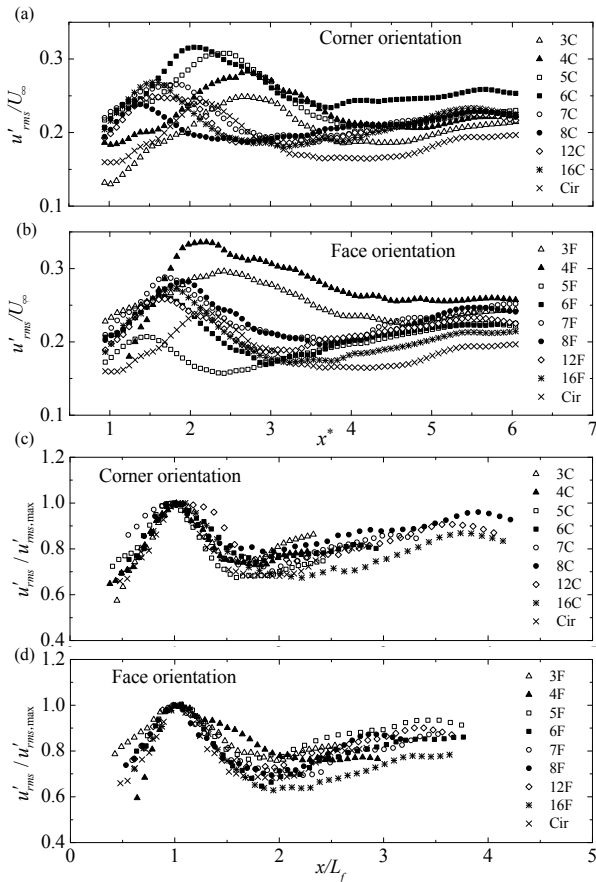

Fig. 14 (a), (b) RMS of streamwise fluctuating velocity u'_{rms} along the centerline at $Re = 1.6 \times 10^4$; (c), (d) Dependence of u'_{rms} / $u'_{rms,\max}$ on x/L_f.

The variation in u'_{rms} along the centerline (Fig. 14a, b) exhibits a similar trend for all cylinders, that is, increasing rapidly to the maximum value $u'_{rms,\max}$ and then decreasing before rising again rather slowly. The largest $u'_{rms,\max}$ occurs at $x^* \approx 2$ for 6C and 4F, cases 8C and 5F are associated with the smallest $u'_{rms,\max}$ that occurs at $x^* \approx 1.3$; the circular cylinder has the lowest u'_{rms} beyond $x^* = 3$. Although the centerline u'_{rms} is significantly different from one cylinder to another, its streamwise variation rescaled with L_f (Fig. 14c, d), at which the oppositely signed vortices interact most

strongly, are almost the same for different cylinders. Indeed, it has been shown that L_f is about the same as L_r, especially for this Re, and $\delta_{1/2}$ reaches the minimum (Fig. 13) at L_f or L_r, with the mean separation streamlines intersect with the centerline. The u'_{rms} then drops to 0.6 $\sim 0.8 \, u'_{rms,\max}$ at $x/L_f \approx 2$. It is plausible that the decrease in the centerline u'_{rms} over this streamwise range is attributed to the steady vortices moving away laterally from the centerline, which is internally consistent with the $\delta_{1/2}$ variation for $1 < x/L_r < 2$ in Fig. 13(c, d). Beyond $x/L_f = 2$, u'_{rms} rises again, regardless of N and the cylinder orientations, though much less rapidly than that for $x/L_f < 1$, probably due to the increased vorticity diffusion and vortex distortion downstream. As the case of $\delta_{1/2}/D_b$ in Fig. 13(c, d), $u'_{rms}/u'_{rms,\max}$ is less dependent on N and the cylinder orientation for $x < 2L_f (\approx 2L_r)$.
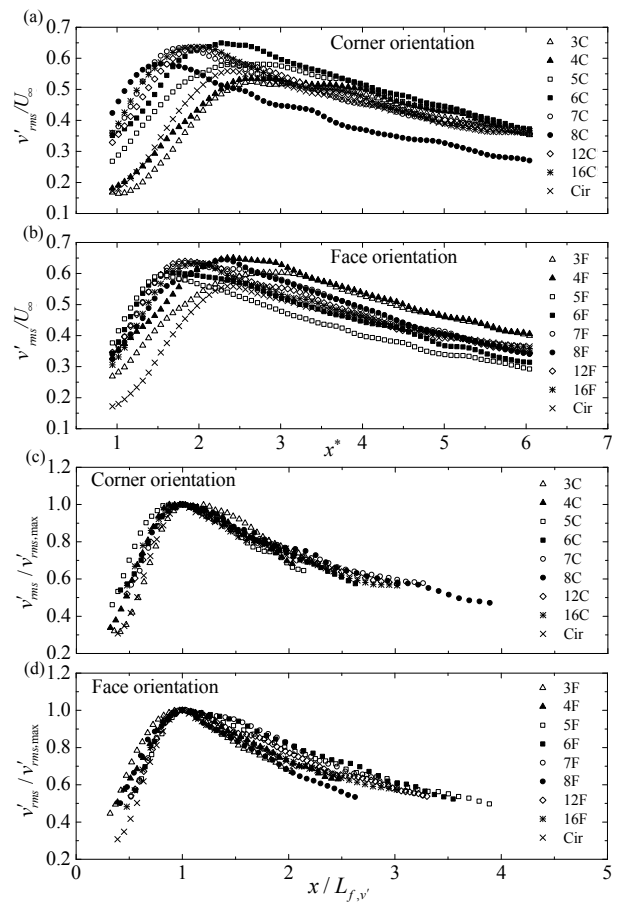

Fig. 15 (a), (b) RMS of the lateral fluctuation velocity v'_{rms} along the centerline at $Re = 1.6 \times 10^4$. (c), (d) Dependence of $v'_{rms}/v'_{rms,\max}$

on $x/L_{f,v'}$.

In distinct contrast to u'_{rms}, the centerline v'_{rms} (Fig. 15a, b) displays only one single peak, that is, v'_{rms} increases rapidly to its maximum $v'_{rms,max}$ and then decays slowly downstream. The v'_{rms} is also different from u'_{rms} in its decay rate which is almost the same for all cylinders and approximately linear with respect x. This is probably due to the combined effect of vortices moving laterally away from the centerline and decaying in strength once beyond the characteristic length $L_{f,v'}$ where $v'_{rms,max}$ occurs. Physically, $v'_{rms,max}$ corresponds to the smallest separation between the oppositely signed vortices. Thus, both L_f and $L_{f,v'}$ are linked to L_r. A comparison between Fig. 15(a, b) and Fig. 14(a, b) indicates that the variation of $L_{f,v'}$ resembles that of L_f, though $L_{f,v'} \gtrsim L_f$, their difference being up to $\sim 0.5D$, such as case 16C. The dependence of the centerline $v'_{rms}/v'_{rms,max}$ on $x/L_{f,v'}$ (Fig. 15c, d) exhibits a better collapse for all cylinders than that of the centerline $u'_{rms}/u'_{rms,max}$ on x/L_f. The result indicates that $L_{f,v'}$ could be also used to define the vortex formation length in the cylinder wake. Fig. 14(c, d) and Fig. 15(c, d) suggest that the near field variation of the centerline $u'_{rms}/u'_{rms,max}$ or $v'_{rms}/v'_{rms,max}$ with x/L_f or $x/L_{f,v'}$ in the wake of a polygonal cylinder can be approximately predicted by that of the circular cylinder.

3.4.2 Scaling of the force coefficients

Xu et al. (2017) found that the corrected flow separation angle ξ is a proper scaling factor for C_D and St of polygonal cylinders for both subcritical and supercritical Re conditions, if transition ever occurs. The ξ is calculated from the actual flow separation angle θ_s, which is the angle between the polygon side upstream of the separation point and the incoming flow direction. The determination of θ_s relies on careful flow visualization around the cylinder surface, which is sometimes difficult due to the high-frequency oscillation of the flow separation points. Therefore, it is of importance to find alternative scaling factors to scale C_D and St as well as $C_{L,rms}$, where subscript rms denotes the root mean square
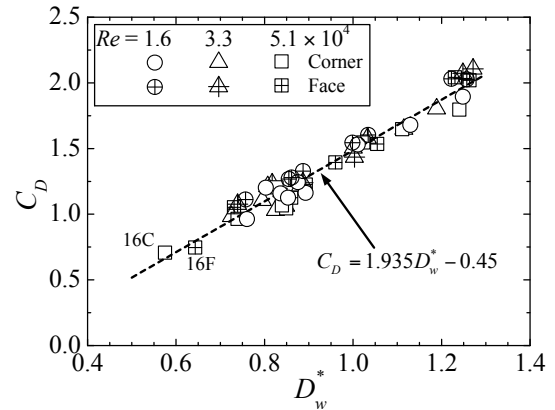
value of instantaneous lift coefficient C_L.

Fig. 16 Dependence of C_D on D_w^* at different Re. The dashed lines are the least square fit to the data of all cylinders.

A connection between C_D on a cylinder and the wake width has been reported previously (e.g. Apelt et al. 1973; Griffin 1995). Griffin (1995) showed that a larger D_w^* was associated with a lower base pressure coefficient C_{pb} and hence larger drag. However, this connection has not been quantified. Indeed, the C_D data can display a good collapse onto a linear curve, viz.

$$C_D = 1.935D_w^* - 0.45, \tag{1}$$

when plotted against D_w^* (Fig. 16), irrespective of N and the cylinder orientation. Since the transition from laminar to turbulence occurs in the boundary layer for cases $N = 12$ and 16, the excellent collapse for all the Re suggests that the correlation equation (1) is valid for the Re range examined, including the polygonal cylinder wake in the supercritical regime (such as 16C and 16F). Wygnanski et al. (1986) demonstrated that the momentum thickness Θ is an important characteristic length scale in the small-deficit wake, i.e., the far wake, and that $2\Theta = C_D D$ by definition. Fig. 16 unveils that D_w^* is an alternative characteristic length scale for the polygonal cylinders. However, being the characteristic wake width defined at the vortex formation length, D_w^* can be readily measured from the near-wake velocity distribution.

Since C_D and ξ were previously found to be linearly correlated by $C_D = 0.0128\xi + 0.9$ (Xu et al. 2017), the empirical relation between D_w^* and ξ can then be derived directly from equation (1), viz.
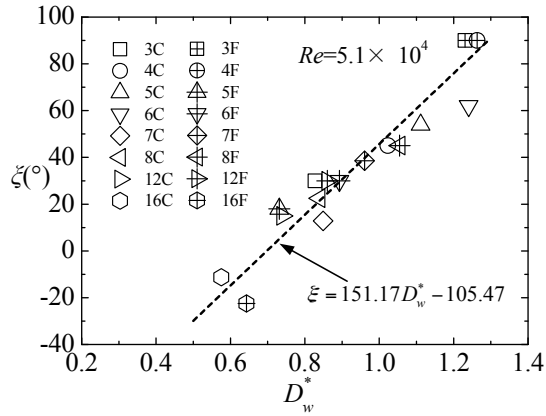
$$\xi = 151.17D_w^* - 105.47. \tag{2}$$

Fig. 17 Relation between D_w^* and ξ at $Re = 5.1\times10^4$.

Fig. 17 compares equation (2) with the experimental data at $Re = 5.1\times10^4$, where ξ is extracted from Xu *et al.* (2017). The significance is that when the flow field information right around the cylinder is unavailable, ξ and hence the averaged flow separation angle θ_s (whose instantaneous value may oscillate randomly) may be estimated from D_w^* via equation (2). Since the relation $C_D = 0.0128\xi + 0.9$ was demonstrated to work for $Re = (2 \sim 10) \times 10^4$, equation (2) is also valid for the same Re range.

The scaling analysis of St turns out to be more challenging. After many trial and error attempts, we define a St^+ as following,

$$St^+ = StD_w^* = f_sD_w/U_\infty. \tag{3}$$

The St^+ data collapse very well for all polygons if plotted against L_f^*, as shown in Fig. 18, regardless of N, the cylinder orientation and Re. The data are least-square-fitted to a second order polynomial, viz.
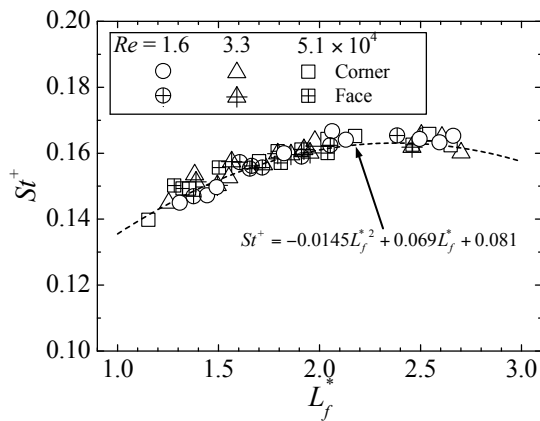
$$St^+ = -0.0145L_f^{*2} + 0.069L_f^* + 0.081. \tag{4}$$

Fig. 18 Dependence of St^+ on L_f^* at different Re. The dashed lines

are the least square fit to the data of all cylinders.

St^+ essentially compromises the observations from St and C_D, which behaved quite differently, and appears insensitive to Re. It may be inferred from the quadratic relation of equation (4) that the maximum $St^+= 0.163$ occurs at $L_f^* = 2.38$. Finding the polygon to yield this maximum St^+ could be of practical significance. It will be demonstrated that D_w scales with the fluctuating lift coefficient in Fig. 19, equation (3) thus suggests that the maximum St^+ may have implication on the most energetic mixing effect or the highest oscillating motion power output given a flexibly mounted cylinder because of the strongest fluctuating lift. However, the theoretical maximum St^+ could be difficult to achieve in reality due to the discretized N. It may occur with a polygon at a particular angle of attack. Determining this angle of attack is beyond the scope of this study and we leave it for a future work.

On the other hand, combining equations (1) and equation (3) with the empirical relation $\zeta=C_D^{0.6}St$ (Xu et al. 2017) may yield $\zeta C_D^{0.4} \sim St^+ = f\left(L_f^*\right)$, where ζ is an empirical constant, about 0.2. This implies that it is possible to use the empirical relations to estimate C_D and hence St from L_f^*, that is, from the information of the streamwise velocity along the centerline.

Hu et al. (2006) found that the sectional circulation Γ_p around their cylinder (square prism) is proportional to C_D. The Kutta-Joukowski lift theorem (Anderson 2010) states that $C_L(t) \propto \Gamma_p$. Since $C_{L,rms}$, calculated from the cyclic oscillation of $C_L(t)$, is proportional to the latter and $C_D \propto D_w^*$, as demonstrated in Fig. 16, one may infer that $C_{L,rms}$ is linearly correlated with D_w^*. Fig. 19 presents the correlation between $C_{L,rms}$ and D_w^* and the data indeed collapse reasonably well, which are least-square-fitted to a linear curve $C_{L,rms} = 0.226D_w^*+0.193$. The data for the configurations of 3C and 4F deviate greatly from the curve. To explain this deviation, we define l_s as the distance from the flow separation point to the leeward surface of the cylinder (see Fig. 20), which approximately indicates the extent of the direct impact of the separated flow on the cylinder

body, i.e., the effect of the negative pressure in the flow separation region on the upper and bottom surface of the cylinder. A larger l_s suggests a larger lift fluctuation given the same Re. Note that $l_s = 0$ for 3C but $l_s = D$ for

4F, representing the two extremes. On the other hand, $l_s = 0.4 \sim 0.8D$ for other polygonal cylinders. Accordingly, 3C and 4F are associated with the minimum and the maximum lift fluctuation (Fig. 19), respectively.
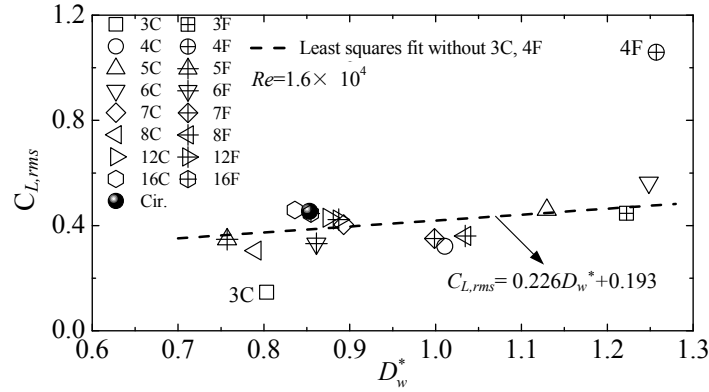

Fig. 19 Relation between D_w^* and $C_{L,rms}$ at $Re = 1.6 \times 10^4$. The dashed line is the least square fit to the data without 3C and 4F.
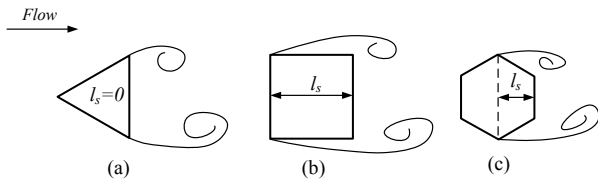

Fig. 20 Definition of l_s. (a) $l_s = 0$ for 3C; (b) $l_s = D$ for 4F; (c) $l_s = 0.5D$ for 6F.

4 Conclusions

In this paper, two sets of scaling parameters are identified: (i) the reverse flow zone length L_r and the recirculation bubble width D_b determined from the time-averaged velocity field $\overline{U}$, (ii) the vortex formation length L_f and the wake width D_w extracted from the fluctuating velocity u'_{rms} field. The mechanism of vortex formation from the polygon surface is reflected uniquely in these length scales. On the other hand, the empirical relations between these scaling factors and various kinematic and dynamic quantities clearly suggest that the understanding of the polygonal cylinder wake could be unified to that of the circular cylinder wake, that is, the shape and orientation information of the polygons is irrelevant as long as appropriate longitudinal and transverse length scales are used. More conclusions are drawn below.

(1) The characteristic properties (U_1, $\delta_{1/2}$, L_r and D_b) of the near wake mean velocity field exhibit a

significant dependence on N and the cylinder orientation. The 8C and 5F cases show the smallest U_1, L_r, D_b and the most rapid centerline velocity recovery for the corner and face orientations, respectively. The results are connected to the small adverse pressure gradient in the reverse flow zone for 8C and 5F cases, due to their very weak vortex strength compared with other cases. On the other hand, the 6C and 4F cases are characterized by the largest vortex strength and adverse pressure gradient in the reverse flow zone, resulting in the smallest velocity recovery rate.

(2) The fluctuating velocities u'_{rms} and v'_{rms} display a great disparity for different N and cylinder orientations. However, the centerline $u'_{rms}/u'_{rms,max}$ collapses reasonably well if x is scaled by L_f. In general, the centerline $u'_{rms}/u'_{rms,max}$ reaches its maximum at the end of the vortex formation, i.e. $x = L_f$, and then declines until $x \approx 2L_f$, followed by a slow rise. The centerline $v'_{rms}/v'_{rms,max}$ displays a reasonable collapse if x is scaled by the characteristic length $L_{f,v'}$ defined as the distance between the cylinder center and the downstream position where the maximum v'_{rms} occurs.

(3) The force coefficients (C_D, $C_{L,rms}$) and Strouhal number (St) all depend heavily on N and the cylinder

orientation. Since U_1, which scales with $D_b \cdot f_s$ and the longitudinal extent of the reverse flow region L_r are closely related to the local absolute instability that governs the vortex shedding process, it is expected that L_r and D_b, behaving similarly to L_f and D_w respectively, are linked to C_D, $C_{L,rms}$ and St. Firstly, C_D is found to be linearly correlated with D_w^*. So is $C_{L,rms}$. The measured data are reasonably fitted to $C_D = 1.935D_w^* - 0.45$ and $C_{L,rms} = 0.226D_w^* + 0.193$, respectively. An alternative Strouhal number $St^+ = StD_w^*$ is also found to scale with L_f^*; the data are fitted very well to $St^+ = -0.0145L_f^{*2} + 0.069L_f^* + 0.081$. Secondly, Xu et al. (2017) found that C_D scales linearly with the corrected flow separation angle ξ. Then, ξ and D_w^* should be linearly correlated, as confirmed presently (Fig. 17). Finally, the empirical relation $\zeta = C_D^{0.6}St$, proposed by Xu et al. (2017), effectively establishes an interrelationship between L_f and D_w. The scaling relations established in this work are independent of N, Re and the cylinder orientation.

References

Alam, M. M., Zhou, Y. & Wang, X. W. (2011) The wake of two side-by-side square cylinders. J. Fluid Mech. 669, 432–471.
https://doi.org/10.1017/S0022112010005288

Anderson, J. (2010) Fundamentals of Aerodynamics (McGraw-Hill Series in Aeronautical and Aerospace Engineering). pp. 280-282. McGraw-Hill Education.

Apelt, C. J., West, G. S., & Szewczyk, A. A. (1973) The effects of wake splitter plates on the flow past a circular cylinder in the range $10^4 <$ Re $< 5 \times 10^4$. J. Fluid Mech. 61(1), 187-198.
https://doi.org/10.1017/S0022112073000649

Bearman P. W. & Obasaju E. D. (1982) An experimental study of pressure fluctuations on fixed and oscillating square-section cylinders. J. Fluid Mech. 119: 297-321.
https://doi.org/10.1017/S0022112082001360

Bloor, M. S. (1964) The transition to turbulence in the wake of a circular cylinder. J. Fluid Mech. 19, 290–304.
https://doi.org/10.1017/S0022112064000726

Carberry, J., Sheridan, J. & Rockwell, D. (2001) Forces and wake modes of an oscillating cylinder. J. Fluids Struct. 15(3-4), 523-532.
https://doi.org/10.1006/jfls.2000.0363

Cetiner, O. & Rockwell, D. (2001) Streamwise oscillations of a cylinder in a steady current. Part 1. Locked-on states of vortex formation and loading. J. Fluid Mech. 427, 1-28.
https://doi.org/10.1017/S0022112000002214

Gerrard, J. H. (1966) The mechanics of the formation region of vortices behind bluff bodies. J. Fluid Mech. 25 (2), 401-413.
https://doi.org/10.1017/S0022112066001721

Griffin, O. M. (1995) A note on bluff-body vortex formation. J. Fluid Mech. 284, 217-224.
https://doi.org/10.1017/S0022112095000322

He, G. S., Li, N. & Wang, J. J. (2014) Drag reduction of square cylinders with cut-corners at the front edges. Exp. Fluids 55(6), 1745.
https://doi.org/10.1007/s00348-014-1745-1

Hu, J. C., Zhou, Y. & Dalton, C. (2006) Effects of the corner radius on the near wake of a square prism. Exp. Fluids 40, 106-118.
https://doi.org/10.1007/s00348-005-0052-2

Huerre, P., & Monkewitz, P. A. (1990) Local and global instabilities in spatially developing flows. Annu. Rev. Fluid Mech. 22(1), 473-537.
https://doi.org/10.1146/annurev.fl.22.010190.002353

Kim, Y. C., Bandi, E.K., Yoshida, A., & Tamura, Y. (2015) Response characteristics of super-tall buildings - Effects of number of sides and helical angle. J. Wind Engng Ind. Aerodyn. 145, 252-262.
https://doi.org/10.1016/j.jweia.2015.07.001

Kim, W., Yoo, J. Y. & Sung, J. (2006) Dynamics of vortex lock-on in a perturbed cylinder wake. Phys. Fluids 18, 074-103.
https://doi.org/10.1063/1.2221350

Monkewitz, P. A. & Nguyen, L. N. (1987) Absolute instability in the near-wake of two-dimensional bluff bodies. J. Fluids Struct. 1(2), 165-184.
https://doi.org/10.1016/S0889-9746(87)90323-9

Nishimura H. & Tanike Y. (2001) Aerodynamic characteristics of fluctuating forces on a circular cylinder. J. Wind Engng Ind. Aerodyn. 89(7-8): 713-723.
https://doi.org/10.1016/S0167-6105(01)00067-8

Qu, Y., Wang, J. J., Sun, M., Feng L. H., Pan, C., Gao Q. & He, G. S. (2017) Wake vortex evolution of square cylinder

with a slot synthetic jet positioned at the rear surface. J. Fluid Mech. 812, 940-965. https://doi.org/10.1017/jfm.2016.833

Shi, X. D. & Feng, L. H. (2015) Control of flow around a circular cylinder by bleed near the separation points. Exp. Fluids 56, (12), 214. https://doi.org/10.1007/s00348-015-2083-7

Tian, Z. W., Niu, H. T. & Wu, Z. N. (2011) Flow past polygons with an odd number of edges. Sci. China Phys. Mech. 54 (4), 683-689. https://doi.org/10.1007/s11433-011-4267-3

Triantafyllou, G. S., Triantafyllou, M. S. & Chryssostomidis, C. (1986) On the formation of vortex streets behind stationary cylinders. J. Fluid Mech. 170, 461-477. https://doi.org/10.1017/S0022112086000976

Unal, M. F. & Rockwell, D. (1988) On vortex formation from a cylinder. part 1. the initial instability. J. Fluid Mech. 190(1), 491-512. https://doi.org/10.1017/S0022112088001429

Wang, L., Alam, M. M. & Zhou, Y. (2018) Two tandem cylinders of different diameters in crossflow: effect of an upstream cylinder on wake dynamics, J. Fluid Mech. 836, 5-42. https://doi.org/10.1017/jfm.2017.735

Wygnanski, I., Champagne, F., & Marasli, B. (1986) On the large-scale structures in two-dimensional, small-deficit, turbulent wakes. J. Fluid Mech. 168, 31-71. https://doi.org/10.1017/S0022112086000289

Xu, S. J., Zhang, W. G., Gan, L., Li, M. G. & Zhou, Y. (2017) Experimental study of flow around polygonal cylinders. J. Fluid Mech. 812, 251-278. https://doi.org/10.1017/jfm.2016.801